

## **Optimization of Si/SiGe heterostructures for large and robust valley splitting in silicon qubits**

Abel Thayil<sup>1</sup>, Lasse Ermoneit<sup>1</sup>, Lars R. Schreiber<sup>2</sup>, Thomas Koprucki<sup>1</sup>,

Markus Kantner<sup>1</sup>

submitted: December 19, 2025

<sup>1</sup> Weierstrass Institute  
Anton-Wilhelm-Amo-Str. 39  
10117 Berlin  
Germany

E-Mail: [abel.thayil@wias-berlin.de](mailto:abel.thayil@wias-berlin.de)  
[lasse.ermoneit@wias-berlin.de](mailto:lasse.ermoneit@wias-berlin.de)  
[thomas.koprucki@wias-berlin.de](mailto:thomas.koprucki@wias-berlin.de)  
[markus.kantner@wias-berlin.de](mailto:markus.kantner@wias-berlin.de)

<sup>2</sup> JARA Institute for Quantum Information,  
Forschungszentrum Jülich GmbH,  
RWTH Aachen University and  
ARQUE Systems GmbH  
52074 Aachen  
Germany

E-Mail: [lars.schreiber@physik.rwth-aachen.de](mailto:lars.schreiber@physik.rwth-aachen.de)

No. 3249  
Berlin 2025



---

2020 *Mathematics Subject Classification.* 35Q40, 35Q81, 35Q93, 65K10, 49M41, 81Q37, 81V65.

*Key words and phrases.* Spin-qubits, quantum computers, quantum dots, semiconductor heterostructures, valleytronics, random alloy fluctuations, perturbation theory, PDE constrained optimization, shape optimization.

This work was funded by the Deutsche Forschungsgemeinschaft (DFG, German Research Foundation) under Germany's Excellence Strategy -- The Berlin Mathematics Research Center MATH+ (EXC-2046/1, project ID: 390685689) and the Cluster of Excellence "Matter and Light for Quantum Computing" (ML4Q, EXC 2004/2, project ID 390534769). M.K. acknowledges helpful discussions with Shalva Amiranashvili.

Edited by  
Weierstraß-Institut für Angewandte Analysis und Stochastik (WIAS)  
Leibniz-Institut im Forschungsverbund Berlin e. V.  
Anton-Wilhelm-Amo-Straße 39  
10117 Berlin  
Germany

Fax: +49 30 20372-303  
E-Mail: [preprint@wias-berlin.de](mailto:preprint@wias-berlin.de)  
World Wide Web: <http://www.wias-berlin.de/>

# Optimization of Si/SiGe heterostructures for large and robust valley splitting in silicon qubits

Abel Thayil, Lasse Ermoneit, Lars R. Schreiber, Thomas Koprucki,  
Markus Kantner

## Abstract

The notoriously low and fluctuating valley splitting is one of the key challenges for electron spin qubits in silicon (Si), limiting the scalability of Si-based quantum processors. In silicon-germanium (SiGe) heterostructures, the problem can be addressed by the design of the epitaxial layer stack. Several heuristic strategies have been proposed to enhance the energy gap between the two nearly degenerate valley states in strained Si/SiGe quantum wells (QWs), *e.g.*, sharp Si/SiGe interfaces, Ge spikes or oscillating Ge concentrations within the QW. In this work, we develop a systematic variational optimization approach to compute optimal Ge concentration profiles that boost selected properties of the intervalley coupling matrix element. Our free-shape optimization approach is augmented by a number of technological constraints to ensure feasibility of the resulting epitaxial profiles. The method is based on an effective mass type envelope function theory accounting for the effects of strain and compositional alloy disorder. Various previously proposed heterostructure designs are recovered as special cases of the constrained optimization problem. Our main result is a novel heterostructure design we refer to as the *modulated wiggle well*, which provides a large deterministic enhancement of the valley splitting along with a reliable suppression of the disorder-induced volatility. In addition, our new design offers a wide-range tunability of the valley splitting controlled by the vertical electric field, which offers new perspectives to engineer switchable qubits with on-demand adjustable valley splitting.

## 1 Introduction

Spin qubits in silicon-germanium (SiGe) heterostructures represent a promising platform for the realization of fully scalable, fault-tolerant quantum computers [1–3]: They combine a very small footprint, long spin coherence times due to the availability of nuclear spin-free isotopes [4–6], weak spin-orbit interaction and compatibility with established semiconductor fabrication technology [7–10]. Experiments have demonstrated state initialization, readout, one and two-qubit gate operations [11–18] as well as quantum error mitigation [19] and correction [20] with high fidelity. Scalable quantum computing architectures require a modular processor design with coherent coupling of distant qubits to overcome crosstalk and quantum dot (QD) wiring limitations [21–24]. As a major step in this direction, coherent qubit transfer across the chip was recently demonstrated using conveyor-mode spin-qubit shuttles [25–28].

A key challenge in strained Si/SiGe quantum wells (QWs) is the existence of two nearly degenerate conduction band valley states that can lead to leakage of quantum information outside of the computational Hilbert space. The energy splitting between the two valleys, *i.e.*, the *valley splitting*, see Fig. 1, is often small (typically 10–100  $\mu\text{eV}$ ) and highly volatile—depending on atomistic details of the Si/SiGe interface and alloy disorder—such that there is a large variability across devices [29–33]. Presently, the valley splitting poses a major bottleneck for silicon spin qubits that critically limits the

scalability of the technology platform towards large-scale quantum computing applications. Several strategies have been proposed to enhance the valley splitting, such as engineering of sharp interfaces [32], Ge-spikes [34, 35], superlattice barriers [36, 37] and oscillating Ge concentrations (“wiggle wells”) [38–42], ideally combined with shear strain engineering [43–45]. Central to these approaches is the design of the epitaxial SiGe layer stack in order to boost the coupling of the two valley states. The inclusion of Ge, however, inevitably leads to alloy fluctuations that cause a statistical broadening of the valley splitting distribution in the device [29, 30, 32, 44, 46–48]. Robust Si/SiGe qubits require a deterministic enhancement of the valley splitting that reliably exceeds the Zeeman splitting across the entire chip to avoid spin-valley hotspots [49–51]. This is especially important for shuttling-based architectures [33, 52–54] and large dense qubit arrays [21, 55], where the variability of the valley splitting is probed over large domains spanning several micrometers. Finally, a low valley splitting limits the fidelity of two-qubit gate operations (since the electrons must reside in a definite valley state) and the Pauli spin blockade read out [56].

In this work, we consider the design of the epitaxial Ge concentration profile as a constrained optimization problem to enhance the valley splitting. Our approach is based on a multi-valley envelope function theory augmented by nonlocal empirical pseudopotential theory that accounts for the effects of strain and alloy disorder [44]. By considering a number of different optimization objectives, we recover a variety of the heuristically known epitaxial profiles in a systematic way, including, *e.g.*, narrow wells and structures with wiggle wells and Ge-spikes. Our main result is a *modulated wiggle well* that outperforms the conventional sinusoidal wiggle well by enhancing the deterministic contribution to the valley splitting while simultaneously reducing the disorder-induced random component.

This paper is organized as follows: In Sec. 2 we derive an expression for the intervalley coupling matrix element in Si/SiGe spin qubits, which is a brief review of the theoretical model from Ref. [44]. In Sec. 3, we describe our variational optimization approach, including the formulation of the cost functional and details on the numerical method. Finally, optimization results are presented and discussed in Sec. 4.

## 2 Theory of Intervalley Coupling

In this section, we summarize the theoretical model for the intervalley coupling matrix element employed in the optimization procedure below in Sec. 3. The model is based on multi-valley envelope function theory augmented by a statistical model to account for random alloy disorder as well as a nonlocal empirical pseudopotential model to account for band structure effects in the presence of strain. Due to the consideration of random alloy disorder, the intervalley coupling strength is regarded as a stochastic quantity throughout this work. Similar effective mass-type models were shown to be in good agreement with atomistic tight-binding models and density functional theory [29, 40, 42]. A comprehensive description of the model can be found in Ref. [44].

### 2.1 Hamiltonian

We consider an electron in a gate-defined QD in a strained Si/SiGe QW grown on the [001] surface. Biaxial strain lifts the degeneracy of the six conduction band valley states and separates the two low-energy Bloch states with wave vectors near  $\mathbf{k} = \pm\mathbf{k}_0 \approx (0, 0, \pm 0.84) \times 2\pi/a_0$  from the other four conduction band valleys [57], see Fig. 1. The remaining two valley states are coupled via valley-orbit interaction at the heterostructure interfaces, which finally lifts their degeneracy. The two-valley envelope

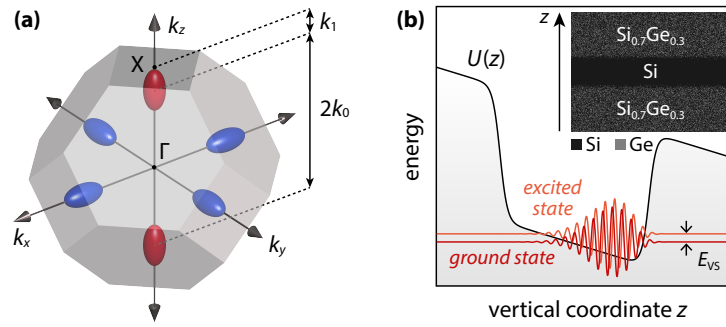


**Fig. 1.** (a) Brillouin zone of the face centered cubic crystal with six valley states along the edges between the  $\Gamma$  point and the six  $X$  points. In biaxially strained Si/SiGe QWs, the four valley states along the  $k_x$  and  $k_y$  directions (blue) are energetically separated from the two low-energy valleys along the  $k_z$  directions (red). (b) Schematic illustration of the ground and excited valley state wave function (including the rapidly oscillating Bloch factors) in the effective confinement potential of a Si/Si<sub>0.7</sub>Ge<sub>0.3</sub> QW. The energy splitting  $E_{VS}$  between the two valley states is usually small in conventional QWs with smooth interfaces. Disorder in the SiGe alloy leads to a significant volatility of the valley splitting. The inset shows a typical realization of alloy disorder in a conventional Si/SiGe QW.

function obeys the stationary, effective mass type Schrödinger equation [39, 43, 44, 58, 59]

$$\begin{pmatrix} H_0(\mathbf{r}) & V_c(\mathbf{r}) \\ V_c^*(\mathbf{r}) & H_0(\mathbf{r}) \end{pmatrix} \begin{pmatrix} \Psi_+(\mathbf{r}) \\ \Psi_-(\mathbf{r}) \end{pmatrix} = E \begin{pmatrix} \Psi_+(\mathbf{r}) \\ \Psi_-(\mathbf{r}) \end{pmatrix}, \quad (1)$$

where  $\Psi_{\pm}$  are the valley-specific envelope wave functions corresponding to the Bloch waves at  $\pm\mathbf{k}_0$ . The diagonal part of the Hamiltonian

$$H_0 = -\frac{\hbar^2}{2m_t} \left( \frac{\partial^2}{\partial x^2} + \frac{\partial^2}{\partial y^2} \right) - \frac{\hbar^2}{2m_l} \frac{\partial^2}{\partial z^2} + U(\mathbf{r}) \quad (2)$$

includes the transverse and longitudinal effective masses  $m_t$  and  $m_l$  as well as the total confinement potential  $U$ . The two valley states are coupled by the interaction Hamiltonian

$$\begin{aligned} V_c(\mathbf{r}) &= e^{-2i\mathbf{k}_0 \cdot \mathbf{r}} u_+^*(\mathbf{r}) u_-(\mathbf{r}) U(\mathbf{r}) \\ &= \sum_{\mathbf{G}, \mathbf{G}'} e^{-i(\mathbf{G} - \mathbf{G}' + 2\mathbf{k}_0) \cdot \mathbf{r}} c_+^*(\mathbf{G}) c_-(\mathbf{G}') U(\mathbf{r}), \end{aligned} \quad (3)$$

where  $\mathbf{G}, \mathbf{G}'$  are reciprocal lattice vectors of the (strained) diamond crystal and  $c_{\pm}(\mathbf{G}) = c_{\pm\mathbf{k}_0}(\mathbf{G})$  are the plane wave expansion coefficients of the conduction band Bloch factors at the respective valley minima  $u_{\pm}(\mathbf{r}) = \sum_{\mathbf{G}} \exp(i\mathbf{G} \cdot \mathbf{r}) c_{\pm}(\mathbf{G})$ .

The total potential reads

$$U(\mathbf{r}) = U_{\text{het}}(\mathbf{r}) + U_{\text{QD}}(x, y) + U_F(z), \quad (4)$$

where  $U_{\text{het}}(\mathbf{r})$  is the heterostructure potential that includes a stochastic component modeling random alloy disorder (see below). The in-plane electrostatic confinement potential due to the gate-defined QD is given by

$$U_{\text{QD}}(x, y) = \frac{m_t}{2} (\omega_x^2 x^2 + \omega_y^2 y^2), \quad (5)$$

where  $\omega_x$  and  $\omega_y$  determine the lateral extension of the QD via  $l_i^2 = \hbar / (m_t \omega_i)$ ,  $i \in \{x, y\}$ . The electric field in vertical direction contributes to the total potential as

$$U_F(z) = -e_0 F z, \quad (6)$$

where  $e_0$  is the elementary charge and  $F$  is the electric field strength. Further contributions to the potential like, *e.g.* electrostatic defects [60] or charge noise are omitted in this work.

We use a nonlocal empirical pseudopotential model [61, 62] accounting for spatially homogeneous strain to compute the effective mass tensor components  $m_t$  and  $m_l$ , Bloch factor expansion coefficients  $c_{\pm}(\mathbf{G})$  and the valley wave vector  $\mathbf{k}_0$  at a given strain tensor. We refer to Ref. [44] for details.

## 2.2 Heterostructure Potential and Random Alloy Disorder

The heterostructure confinement potential is modeled as a random field following a scaled Bernoulli distribution

$$U_{\text{het}}(\mathbf{r}) = \Delta E_c \Omega_a \sum_i N_i \delta(\mathbf{r} - \mathbf{R}_i) \quad (7)$$

where  $N_i \sim \text{Bernoulli}(p = X(\mathbf{R}_i))$  describes the probability of finding a Ge atom at the lattice position  $\mathbf{R}_i$ . Moreover,  $\Omega_a$  is the atomic volume and  $\Delta E_c$  is the conduction band offset for Ge atoms in a Si background lattice. We assume a layered (one-dimensional) Ge concentration profile such that  $X(\mathbf{r}) = X(z)$  depends only on the vertical coordinate. Then, the deterministic component (*i.e.*, the mean) of the heterostructure potential is directly proportional to the Ge epitaxial profile

$$\langle U_{\text{het}}(\mathbf{r}) \rangle = U_{\text{QW}}(z) = \Delta E_c X(z). \quad (8)$$

The random component of the heterostructure potential

$$\delta U_{\text{het}}(\mathbf{r}) = U_{\text{het}}(\mathbf{r}) - U_{\text{QW}}(z) \quad (9)$$

has zero mean  $\langle \delta U_{\text{het}}(\mathbf{r}) \rangle = 0$  by construction and a Delta-like covariance function

$$\langle \delta U_{\text{het}}(\mathbf{r}) \delta U_{\text{het}}(\mathbf{r}') \rangle = (\Delta E_c)^2 \Omega_a X(z) (1 - X(z)) \delta(\mathbf{r} - \mathbf{r}'). \quad (10)$$

Throughout this paper, we assume an epitaxial profile of the form  $X(z) = X_{\text{QW}}(z) + x(z)$ . Here,

$$X_{\text{QW}}(z) = X_b (1 - \Xi(z)) \quad (11)$$

is a fixed Ge concentration profile describing a smoothed step-like QW, which is supplemented by a variable modification  $x(z)$  subject to a variational optimization problem described in Sec. 3. The barrier Ge concentration is fixed to  $X_b = 0.3$  and the QW indicator function describing the shape and position of the QW reads

$$\Xi(z) = \frac{1}{2} \left( \tanh\left(\frac{z + h/2}{\sigma_l}\right) - \tanh\left(\frac{z - h/2}{\sigma_u}\right) \right). \quad (12)$$

Here,  $h$  is the thickness of the QW and  $\sigma_l$  and  $\sigma_u$  describe the width of the lower and upper interface, respectively. Parameter values used in the numerical simulations are listed in Tab. 1.

## 2.3 Statistical Distribution of the Intervalley Coupling Parameter

Following first-order degenerate perturbation theory [59], a perturbative expression for the intervalley coupling parameter is obtained as [44]

$$\begin{aligned} \Delta &= \int d^3r e^{-2i\mathbf{k}_0 \cdot \mathbf{r}} u_+^*(\mathbf{r}) u_-(\mathbf{r}) U(\mathbf{r}) \Psi_0^2(\mathbf{r}) \\ &= \sum_{\mathbf{G}, \mathbf{G}'} c_+^*(\mathbf{G}) c_-(\mathbf{G}') \int d^3r e^{-i(\mathbf{G} - \mathbf{G}' + 2\mathbf{k}_0) \cdot \mathbf{r}} U(\mathbf{r}) \Psi_0^2(\mathbf{r}). \end{aligned} \quad (13)$$

Here, both the intervalley coupling (3) and the random alloy fluctuations (9) were assumed to be weak. Moreover,  $\Psi_0(\mathbf{r})$  is the ground state envelope wave function satisfying the (unperturbed) single-valley eigenvalue problem for the mean potential  $\langle U(\mathbf{r}) \rangle$  (i.e., without random alloy fluctuations)

$$\hat{H}^{(0)}(\mathbf{r}) \Psi_0(\mathbf{r}) = E_0 \Psi_0(\mathbf{r}),$$

where the single-valley Hamiltonian reads

$$\hat{H}^{(0)}(\mathbf{r}) = -\frac{\hbar^2}{2m_t} \left( \frac{\partial^2}{\partial x^2} + \frac{\partial^2}{\partial y^2} \right) - \frac{\hbar^2}{2m_l} \frac{\partial^2}{\partial z^2} + \langle U(\mathbf{r}) \rangle,$$

and  $\langle U(\mathbf{r}) \rangle = U_{\text{QW}}(z) + U_F(z) + U_{\text{QD}}(x, y)$  is the deterministic component of the confinement potential.

The intervalley coupling parameter  $\Delta$  is highly sensitive to strain. In fact, deformations of the diamond lattice structure are required to unlock an important interaction mechanism for the coupling of valley states in neighboring Brillouin zones [43, 44]. Throughout this work we assume biaxial strain  $\varepsilon_{\parallel} = 1.14\%$ ,  $\varepsilon_{\perp} = -0.88\%$  induced by the pseudomorphic lattice matched growth of the SiGe/Si/SiGe QW [44, 63] and additional spatially homogeneous shear strain  $\varepsilon_s = 0.1\%$  along the [110] direction. The total strain tensor reads

$$\varepsilon = \begin{pmatrix} \varepsilon_{\parallel} & \varepsilon_s & 0 \\ \varepsilon_s & \varepsilon_{\parallel} & 0 \\ 0 & 0 & \varepsilon_{\perp} \end{pmatrix}.$$

In the computation of the intervalley coupling strength, the strain enters via modifications of the reciprocal lattice vectors and the Bloch factors computed from the empirical pseudopotential model [44].

Since the heterostructure potential (7) includes a deterministic and a random component, the same holds true for the intervalley coupling parameter

$$\Delta = \Delta_{\text{det}} + \Delta_{\text{rand}}.$$

The deterministic part is determined by the mean potential

$$\Delta_{\text{det}} = \langle \Delta \rangle = \int d^3r e^{-2i\mathbf{k}_0 \cdot \mathbf{r}} u_+^*(\mathbf{r}) u_-(\mathbf{r}) \langle U(\mathbf{r}) \rangle \Psi_0^2(\mathbf{r}), \quad (14)$$

whereas characteristic alloy disorder encoded in the stochastic potential fluctuations (9) governs the random component

$$\begin{aligned} \Delta_{\text{rand}} &= \Delta - \langle \Delta \rangle \\ &= \int d^3r e^{-2i\mathbf{k}_0 \cdot \mathbf{r}} u_+^*(\mathbf{r}) u_-(\mathbf{r}) \delta U_{\text{het}}(\mathbf{r}) \Psi_0^2(\mathbf{r}). \end{aligned}$$

Using the central limit theorem, it can be shown that  $\Delta$  obeys a complex normal distribution [44]

$$\Delta \sim \text{ComplexNormal}(\Delta_{\text{det}}, \Gamma, C)$$

with the covariance  $\Gamma$  and the pseudo-covariance  $C$  given as

$$\Gamma = \langle |\Delta_{\text{rand}}|^2 \rangle, \quad C = \langle \Delta_{\text{rand}}^2 \rangle. \quad (15)$$

Formulas used to evaluate the deterministic component  $\Delta_{\text{det}}$ , covariance  $\Gamma$  and pseudo-covariance  $C$  for a layered epitaxial profile  $X(z)$  are given in Appendix A. The pseudo-covariance is typically much smaller than the covariance  $|C| \ll \Gamma$ , such that the distribution law of  $\Delta$  is well described by the circular approximation with independent, normally distributed real and imaginary parts

$$\begin{aligned} \text{Re}(\Delta) &\sim \text{Normal} \left( \mu = \text{Re}(\Delta_{\text{det}}), \sigma^2 = \frac{1}{2}\Gamma \right), \\ \text{Im}(\Delta) &\sim \text{Normal} \left( \mu = \text{Im}(\Delta_{\text{det}}), \sigma^2 = \frac{1}{2}\Gamma \right). \end{aligned}$$

Using this approximation, the valley splitting  $E_{\text{VS}} = 2|\Delta|$  is found to obey a Rice distribution [30, 40, 44]

$$E_{\text{VS}} \sim \text{Rice}(\nu = 2|\Delta_{\text{det}}|, \sigma^2 = 2\Gamma). \quad (16)$$

The mean of the Rice distribution is given as [44]

$$\langle E_{\text{VS}} \rangle = \sqrt{\pi\Gamma} f \left( \frac{|\Delta_{\text{det}}|^2}{2\Gamma} \right), \quad (17)$$

where  $f(x) = e^{-x}((1+2x)I_0(x) + 2xI_1(x))$  and  $I_\nu(\cdot)$  denotes the modified Bessel function of first kind. The variance is obtained as

$$\text{Var}(E_{\text{VS}}) = 4\Gamma \left( 1 + \frac{|\Delta_{\text{det}}|^2}{\Gamma} \right) - \langle E_{\text{VS}} \rangle^2. \quad (18)$$

Finally, we introduce *deterministic component ratio*

$$Q = \frac{2|\Delta_{\text{det}}|}{\langle E_{\text{VS}} \rangle} = 2\sqrt{\frac{2}{\pi}} \frac{\zeta}{f(\zeta^2)} \quad \text{with} \quad \zeta = \frac{|\Delta_{\text{det}}|}{\sqrt{2\Gamma}}, \quad (19)$$

which quantifies the share of the deterministic component on the mean valley splitting (arising from both deterministic and disorder-induced contributions, see Eq. (17)). If the deterministic component dominates over the magnitude of the random component  $\zeta \gg 1$ , the deterministic component ratio approaches unity  $Q \rightarrow 1$ . On the contrary, low values of  $Q$  indicate that the mean valley splitting is dominated by disorder-induced contributions. At  $\zeta \approx 0.3507$ , both the deterministic and the random component contribute equally to the expected valley splitting such that  $Q = 1/2$ .

### 3 Epitaxial Profile Optimization

In Si/SiGe heterostructures, the intervalley coupling matrix element can be tailored by the design of the epitaxial layer stack. Different heuristics for enhancement of the magnitude of the valley splitting were recently discussed in the literature, including wiggle wells [38–40, 43, 44], sharp interfaces [32], Ge spikes [34, 40], narrow wells [40] and uniform Ge concentrations in the QW [30, 40, 52]. All these Ge concentration profiles affect both the deterministic and the random component of the valley coupling parameter in a specific way.

In this section, we address the design of the epitaxial Ge concentration profile as a variational optimization problem to compute optimized epitaxial profiles that enhance selected properties of the intervalley coupling parameter. To this end, we consider a Ge concentration profile of the form

$$X(z) = X_{\text{QW}}(z) + x(z),$$

Symbol	Description	Value
$a_0$	Si lattice constant	0.543 nm
$\Delta E_c$	Si/Ge conduction band offset	0.5 eV
$\Omega_a$	atomic volume	$(a_0/2)^3$
$k_0$	valley wave number	$0.8394 \times 2\pi/a_0$
$k_1$	see Eq. (31)	$0.1694 \times 2\pi/a_0$
$m_t$	transverse effective mass	$0.209 m_0$
$m_l$	longitudinal effective mass	$0.909 m_0$
$h$	thickness of the QW domain	75 ML
$\sigma_u, \sigma_l$	upper and lower interface width	0.5 nm
$X_b$	nominal Ge concentration in barrier	0.3
$\hbar\omega_x, \hbar\omega_y$	circular QD orbital energy splitting	3 meV
$F$	vertical electric field	5 mV/nm

**Tab. 1.** Parameters used in the numerical simulations. A complete list of parameters including also the empirical pseudopotential model is given in Ref. [44]. Here,  $m_0$  is the vacuum electron mass and ML =  $a_0/4$  is the silicon monolayer thickness.

where  $X_{\text{QW}}(z)$  is a fixed QW profile (smoothed step function, see Sec. 2.2) and  $x(z)$  is a modification subject to optimization. The epitaxial profile modification implies a corresponding modification of the potential energy according to Eq. (7).

### 3.1 Optimization Objectives

We consider a number of different optimization objectives. In each case, we seek to minimize a non-negative cost functional involving combinations of the deterministic contribution to the valley splitting  $\nu(x, \psi_0) = 2|\Delta_{\text{det}}(x, \psi_0)|$  and the disorder-induced contribution quantified by the covariance  $\Gamma(x, \psi_0)$ . All numerical computations are based on the separation ansatz described in Appendix A, which reduces the problem to an effective one-dimensional Schrödinger problem depending only on the vertical component  $\psi_0(z)$  of the envelope wave function determined by the Ge concentration profile  $x(z)$ .

The different objectives under consideration read:

- (A) Maximization of the deterministic component

$$J_0^{(A)}(x, \psi_0) = \frac{E_{\text{ref}}}{\nu(x, \psi_0)},$$

where the deterministic contribution to the valley splitting is  $\nu(x, \psi_0) = 2|\Delta_{\text{det}}(x, \psi_0)|$ .

- (B) Minimization of the ratio between disorder-induced and deterministic components

$$J_0^{(B)}(x, \psi_0) = \frac{\sqrt{2\Gamma(x, \psi_0)}}{\nu(x, \psi_0)} = \frac{1}{2\zeta(x, \psi_0)}$$

to maximize the *reliable enhancement*. As the deterministic component ratio  $Q$  is a monotonous function of  $\zeta$ , see Eq. (19), this objective simultaneously covers the maximization of  $Q$ .

(C) Minimization of the disorder-induced random component

$$J_0^{(C)}(x, \psi_0) = \frac{\sqrt{2\Gamma(x, \psi_0)}}{E_{\text{ref}}}$$

for reduction of the valley splitting volatility.

Some of the cost functionals include an arbitrary reference energy set to  $E_{\text{ref}} = 1 \text{ meV}$  for non-dimensionalization. The optimization objectives  $J_0$  are supplemented by further constraints, leading to the total cost functional described in the following section.

### 3.2 Cost Functional

We consider a cost functional for minimization consisting of a number of additive components capturing the optimization objective and constraints. The total cost functional reads

$$J(x, \psi_0, E_0, \chi, \kappa) = J_0(x, \psi_0) + J_1(x, \psi_0, \chi, E_0) + J_2(\kappa, \psi_0) + J_3(x) + J_4(x), \quad (20)$$

where  $J_0(x, \Psi_0)$  is the figure of merit (see Sec. 3.1 above) that captures the key objective for optimization, depending on the Ge epitaxial profile  $x$  and the ground state envelope wave function  $\psi_0$ .

The first constraint ensures that the envelope wave function  $\psi_0$  is an eigenfunction of the Schrödinger eigenvalue problem

$$J_1(x, \psi_0, \chi, E_0) = \int dz \chi(z) \left( \hat{H}^{(0)} - E_0 \right) \psi_0(z),$$

where the deterministic, single-valley Hamiltonian for the longitudinal problem includes the unknown Ge epitaxial profile  $x(z)$  as a variable contribution to the potential energy

$$\hat{H}^{(0)} = -\frac{\hbar^2}{2m_l} \frac{\partial^2}{\partial z^2} + \Delta E_c (X_{\text{QW}}(z) + x(z)) + U_F(z). \quad (21)$$

The ground state wave function  $\psi_0$  and energy level  $E_0$  are selected via suitable heuristics<sup>1</sup>. As the Hamiltonian (21) is real, we assume real-valued eigenfunctions  $\psi_0$  throughout this paper. Finally,  $\chi(z)$  is a (real-valued) adjoint wave function that plays the role of a space-dependent Lagrange multiplier.

The next term in the cost functional

$$J_2(\kappa, \Psi_0) = \kappa \left( 1 - \int dz \psi_0^2(z) \right)$$

enforces normalization of the wave function using a Lagrange multiplier  $\kappa$ . This constraint is indispensable to ensure uniqueness of the optimum and solvability of the adjoint state equation, see Sec. 3.4 below.

The admissible range for the local Ge concentration must be limited by lower and upper bounds  $x_{\text{min}} \leq X(z) \leq x_{\text{max}}$ , where the total epitaxial profile  $X(z) = X_{\text{QW}}(z) + x(z)$  consists of the fixed QW profile  $X_{\text{QW}}(z)$  and the modification  $x(z)$ , which is subject to the free-shape optimization

<sup>1</sup>In the presence of electric fields, we always select the lowest energy bound state that has a strong overlap with the (tilted) QW domain.

problem. We choose  $x_{\min} = 0$  and  $x_{\max} = X_b$ . This requirement is included in the cost functional via the penalty term

$$J_3(x) = \frac{\alpha}{h} \int dz g(X_{\text{QW}}(z) + x(z)),$$

where the function

$$g(x) = \begin{cases} x_{\min} - x & x < x_{\min}, \\ 0 & x_{\min} \leq x \leq x_{\max}, \\ x - x_{\max} & x > x_{\max}. \end{cases}$$

penalizes values of  $x$  outside of the admissible range. The parameter  $\alpha$  is a penalty value (taken to be large). If the epitaxial profile is within the admissible range, the contribution to the cost functional vanishes.

Finally, the overall Ge content in the QW shall be fixed at a target Ge concentration  $x_{\text{Ge}}$ , which is enforced by a second penalty term

$$J_4(x) = \frac{\beta}{2} (\bar{X}(x) - x_{\text{Ge}})^2$$

with another penalty value  $\beta$ . Here,  $\bar{X}$  quantifies the mean Ge concentration in the QW

$$\bar{X}(x) = \frac{1}{h} \int dz \Xi(z) (X_{\text{QW}}(z) + x(z)). \quad (22)$$

In the optimization procedure, the admissible amount  $x_{\text{Ge}}$  of Ge must be distributed within the QW to minimize the overall cost functional while respecting all constraints.

### 3.3 Variational Minimization and Optimality Conditions

We seek for a minimum of the cost functional by considering a small variation of the epitaxial profile  $x(z) \rightarrow x(z) + \delta x(z)$ , which induces a variation of the ground state envelope wave function  $\psi_0 \rightarrow \psi_0 + \delta\psi_0$ , the ground state energy level  $E_0 \rightarrow E_0 + \delta E_0$  and the Lagrange multipliers  $\chi(z) \rightarrow \chi(z) + \delta\chi(z)$  and  $\kappa \rightarrow \kappa + \delta\kappa$ . The condition for the minimum

$$\begin{aligned} 0 &\stackrel{!}{=} \delta J(x, \psi_0, E_0, \chi, \kappa) \\ &= J(x + \delta x, \psi_0 + \delta\psi_0, E_0 + \delta E_0, \chi + \delta\chi, \kappa + \delta\kappa) - J(x, \psi_0, E_0, \chi, \kappa) \end{aligned}$$

leads to

$$\begin{aligned} \delta J &= \int dz \left[ \frac{\delta J_0(x, \psi_0)}{\delta x} + \Delta E_c \chi(z) \psi_0(z) + \frac{\alpha}{h} g'(X(z)) \right. \\ &\quad \left. + \frac{\beta}{h} (\bar{X}(x(z)) - x_{\text{Ge}}) \Xi(z) \right] \delta x(z) \\ &\quad + \int dz \left[ \frac{\delta J_0(x, \psi_0)}{\delta \psi_0} - 2\kappa \psi_0(z) + (\hat{H}^{(0)} - E_0) \chi(z) \right] \delta \psi_0(z) \\ &\quad + \int dz \delta \chi(z) (\hat{H}^{(0)} - E_0) \psi_0(z) \\ &\quad - \delta E_0 \int dz \chi(z) \psi_0(z) + \delta \kappa \left( 1 - \int dz \psi_0^2(z) \right). \end{aligned}$$

From the optimality condition  $\delta J = 0$ , we extract a number of necessary conditions:

- (i) Stationary Schrödinger equation (since  $\delta\chi$  is free): The ground state wave function and energy level must be an eigenstate of the single-valley Hamiltonian (21) including the adapted epitaxial profile

$$\hat{H}^{(0)}\psi_0(z) = E_0\psi_0(z). \quad (23a)$$

- (ii) Normalization (since  $\delta\kappa$  is free): The ground state wave function must be normalized over the full domain

$$\int dz \psi_0^2(z) = 1. \quad (23b)$$

- (iii) Adjoint state equation (since  $\delta\psi_0$  is free): The adjoint solves the linear Schrödinger-type equation with inhomogeneous right hand side depending on the ground state wave function

$$\left(\hat{H}^{(0)} - E_0\right)\chi(z) = 2\kappa\psi_0(z) - \frac{\delta J_0(x, \psi_0)}{\delta\psi_0}. \quad (23c)$$

- (iv) Orthogonality condition (since  $\delta E_0$  is free): The adjoint wave function must be orthogonal to the ground state envelope wave function

$$\int dz \chi(z) \psi_0(z) = 0. \quad (23d)$$

When the conditions (i)–(iv) are satisfied, the gradient of the cost functional with respect to the epitaxial profile is given as

$$\begin{aligned} \frac{\delta J(x, \psi_0)}{\delta x} &= \frac{\delta J_0(x, \psi_0)}{\delta x} + \Delta E_c \chi(z) \psi_0(z) \\ &+ \frac{\alpha}{h} g'(X_{\text{QW}}(z) + x(z)) + \frac{\beta}{h} (\bar{X}(x(z)) - x_{\text{Ge}}) \Xi(z). \end{aligned} \quad (24)$$

The gradient is employed to iteratively update the epitaxial profile modification  $x(z)$  until convergence, see Sec. 3.6. Next to the direct derivative of the key objective functional  $J_0$  with respect to the Ge concentration profile, the gradient involves corrections due to the side constraints  $J_1$  (eigenstate constraint),  $J_3$  (Ge budget) and  $J_4$  (admissible Ge range).

### 3.4 Solution of the Adjoint State Equation

The operator on the left hand side of the adjoint state equation (23c) is rank deficient since  $E_0$  is an eigenvalue of  $\hat{H}^{(0)}$ . Thus, the operator  $(\hat{H}^{(0)} - E_0)$  is not invertible (zero eigenvalue) and care must be taken when solving (23c) for the adjoint wave function  $\chi(z)$ . We emphasize that the latter is necessary to compute the gradient (24) driving the minimization procedure.

The problem (23c) is solvable, if the right hand side has no component along the eigenspace of  $E_0$  (Fredholm alternative). By projecting Eq. (23c) on the ground state envelope wave function (from the left), we obtain by using Eqs. (23a) and (23b) the condition

$$\underbrace{\int dz \psi_0(z) (\hat{H}^{(0)} - E_0) \chi(z)}_{=0} = 2\kappa \underbrace{\int dz \psi_0^2(z)}_{=1} - \int dz \psi_0(z) \frac{\delta J_0(x, \psi_0)}{\delta\psi_0}.$$

Solving this for the Lagrange multiplier  $\kappa$  yields

$$\kappa = \frac{1}{2} \int dz \psi_0(z) \frac{\delta J_0(x, \psi_0)}{\delta \psi_0}, \quad (25)$$

which ensures feasibility (but not yet uniqueness) of the solution. Substituting (25) in (23c), the adjoint state equation becomes

$$\left( \hat{H}^{(0)} - E_0 \right) \chi(z) = R(z), \quad (26)$$

where the modified right hand side

$$R(z) = \psi_0(z) \int dz' \psi_0(z') \frac{\delta J_0(x(z'), \psi_0(z'))}{\delta \psi_0} - \frac{\delta J_0(x(z), \psi_0(z))}{\delta \psi_0}.$$

is orthogonal to the envelope wave function by construction:

$$\int dz \psi_0(z) R(z) = 0.$$

Finally, an explicit solution of Eq. (26) is constructed by expanding the adjoint wave equation in the complete, orthonormal eigenbasis  $\{\psi_n, E_n\}$  of  $\hat{H}^{(0)}$

$$\chi(z) = \sum_n a_n \psi_n(z),$$

which allows to formulate the solution via a Green's function

$$\chi(z) = \int dz' G(z, z') R(z'). \quad (27)$$

The expansion coefficients  $a_n$  for  $n \neq 0$  are uniquely determined by Eq. (26) and obtained as

$$a_n = \frac{1}{E_n - E_0} \int dz \psi_n(z) R(z) \quad (n \neq 0).$$

The missing component  $a_0$  is fixed by the orthogonality condition (23d) and obtained as  $a_0 = 0$ . Finally, this yields

$$G(z, z') = \sum_{n \neq 0} \frac{\psi_n(z) \psi_n(z')}{E_n - E_0}. \quad (28)$$

Thus, accurate computation of the gradient (24) is computationally expensive, as it involves complete diagonalization of the single-valley Hamiltonian (21).

### 3.5 Spectral Constraint

Without further constraints on the epitaxial profile, the optimization algorithm will in most cases converge to rapidly oscillating profiles dominated by a Fourier component at wave number  $2k_0$  (short-period wiggle-well). This period boosts the direct coupling of the two valley states within the same Brillouin zone [39, 42, 44] and thus leads to large enhancements of the valley splitting. This high modulation frequency of the Ge concentration is very close to the atomic monolayer thickness and therefore hard to realize in practice. In order focus on epitaxially feasible heterostructures [41], we need to rule out these

rapidly modulated solutions. To this end, we impose a spectral constraint blocking out high frequency components by replacing

$$x(z) \rightarrow \tilde{x}(z) = \Xi(z) x_K(z), \quad (29)$$

in the cost functional, where  $\Xi(z)$  is the indicator function, see Eq. (12), and

$$\begin{aligned} x_K(z) &= (K * x)(z) = \int dz' K(z - z') x(z') \\ &= \int \frac{dk}{2\pi} e^{-ikz} K(k) x(k) \end{aligned}$$

is a convolution with a filter function  $K$ . Throughout this work, we choose a rectangular low-pass filter with Fourier representation

$$K(k) = \Theta(k_c - |k|),$$

where  $k_c$  is the cutoff frequency and  $\Theta$  is the Heaviside step function. The filtered profile is multiplied with the QW indicator function (12) to suppress oscillations outside of the QW domain. For slowly changing Ge concentration profiles localized within the QW domain, the substitution (29) keeps the input profile practically invariant.

By carrying out this replacement directly on the level of the cost functional

$$J(x) \rightarrow J(\tilde{x}(z)) = J(\Xi(z) (K * x)(z)),$$

the corresponding gradient is obtained as

$$\begin{aligned} \frac{\delta J(\tilde{x}(z))}{\delta \tilde{x}(z)} &= \left( K * \left[ \Xi \frac{\delta J(x)}{\delta x} \right] \right) (z) \\ &= \int dz' K(z - z') \Xi(z') \frac{\delta J(x(z'))}{\delta x(z')}. \end{aligned} \quad (30)$$

Hence, the gradient of the modified functional is obtained from the gradient of the original functional after multiplication with the indicator function  $\Xi$  and subsequent low-pass filtration, *i.e.*, opposite ordering compared to Eq. (29). We point out that simple low-pass filtering of the gradient alone (which is a frequently chosen heuristic to block out undesired frequency components in optimization problems [64, 65]) without corresponding modification of the cost functional will lead to a mismatch of function and gradient. This can drastically degrade or even inhibit the convergence of the gradient-based minimization method used here. Throughout this work, the substitutions (29) and (30) are tacitly employed everywhere and not explicitly indicated by notation.

### 3.6 Numerical Optimization Method

Since the ground state wave function  $\psi_0(z) = \psi_0(x(z))$  is uniquely determined by the epitaxial profile  $x(z)$  via Eq. (23a), the cost functional can be written as a functional of the Ge concentration profile only  $J(x, \psi_0) \rightarrow J(x)$ . To linear order, an update  $\Delta x = \Delta x(z)$  of the epitaxial profile leads to

$$J(x + \Delta x) = J(x) + \int dz \frac{\delta J(x(z))}{\delta x} \Delta x(z) + O(\Delta x^2).$$

In order to obtain a reduction of the cost functional  $J(x + \Delta x) < J(x)$ , the update is chosen as

$$\Delta x(z) = - \int dz' B(z, z') \frac{\delta J(x(z'))}{\delta x},$$

where the functional derivative is computed according to Eq. (24) and  $B(z, z')$  positive definite.

We employ the L-BFGS method with a Wolfe line search [66] for numerical optimization of the cost functional (20). The method iteratively constructs low-rank approximations of the inverse Hessian  $B$  to achieve superlinear convergence. The method is restarted multiple times after every 100 iterations, with the penalty value  $\beta$  being increased incrementally from  $10^4$  to  $10^6$ . The penalty value to enforce the admissible Ge range is fixed to  $\alpha = 10^5$ . We use a limited memory of the 20 most recent gradients to approximate the quasi-Hessian inverse in each step.

## 4 Optimization Results

The results of the numerical optimization of cost functionals with objectives (A)–(C) are shown in Fig. 2 (a)–(d) and discussed in the following. Parameters used are listed in Tab.

### 4.1 Modulated Wiggle Well

When optimizing for the maximization of the deterministic component (A) or reliable enhancement (B), the numerical procedure converges to an oscillating Ge concentration profile with a dominant wave number near  $2k_1$ , where

$$k_1 = \frac{2\pi}{a_0} (1 - \varepsilon_{z,z}) - k_0 \quad (31)$$

is the reciprocal space distance from the valley minimum to the (strained) Brillouin zone edge. This corresponds to a wave length of  $\lambda = \pi/k_1 \approx 1.6 \text{ nm} \approx 11.8 \text{ ML}$ , see Fig. 2 (a)–(b). This type of Ge concentration profile is closely related to the *long-period wiggle well*, which will be denoted as *conventional wiggle well* in the following, that has been extensively discussed in the literature [38–41, 43, 44, 67]. The periodicity of the heterostructure potential boosts the coupling of the valley states in neighboring Brillouin zones separated by  $2k_1$  in reciprocal space, which is in resonance with the epitaxial profile modulation. The conventional wiggle well with sinusoidal Ge concentration profile is shown in Fig. 2 (e) for reference.

The epitaxial profiles that satisfy our optimization objectives (A) or (B) are referred to as *modulated wiggle wells*. These structures differs from the conventional wiggle well by a modulation of the Ge concentration amplitude, which is optimized for a particular electric field in growth direction. The envelope wave function of the ground state electrons in these structures is stretched out over the entire QW domain in order to enhance the overlap of the wave function with the Ge modulations. This way, the resonance in the intervalley coupling parameter is boosted in an optimal way, leading to a strong enhancement of the deterministic component  $\nu$ . This is reflected by the strong peak in the power spectral density (PSD) of the product

$$S(z) = (\Delta E_c X(z) + U_F(z)) \psi_0^2(z), \quad (32)$$

which enters Eq. (33), that is shown in the third column of Fig. 2 (a)–(b). Both modulated wiggle wells are very similar, despite different optimization objectives are pursued. In fact, the modulated wiggle well (A) has a slightly larger deterministic component  $\nu$  than the modulated wiggle well (B), which can be seen from the larger distance of the center of the probability density of the intervalley coupling parameter  $\Delta$  from the origin of the complex plane, see fourth column of Fig. 2 (a)–(b). In turn, the modulated wiggle well (B) provides an enhanced ratio of (large) deterministic and (small) disorder-induced contributions, simultaneously. Both structures outperform the conventional wiggle well at the same Ge content.

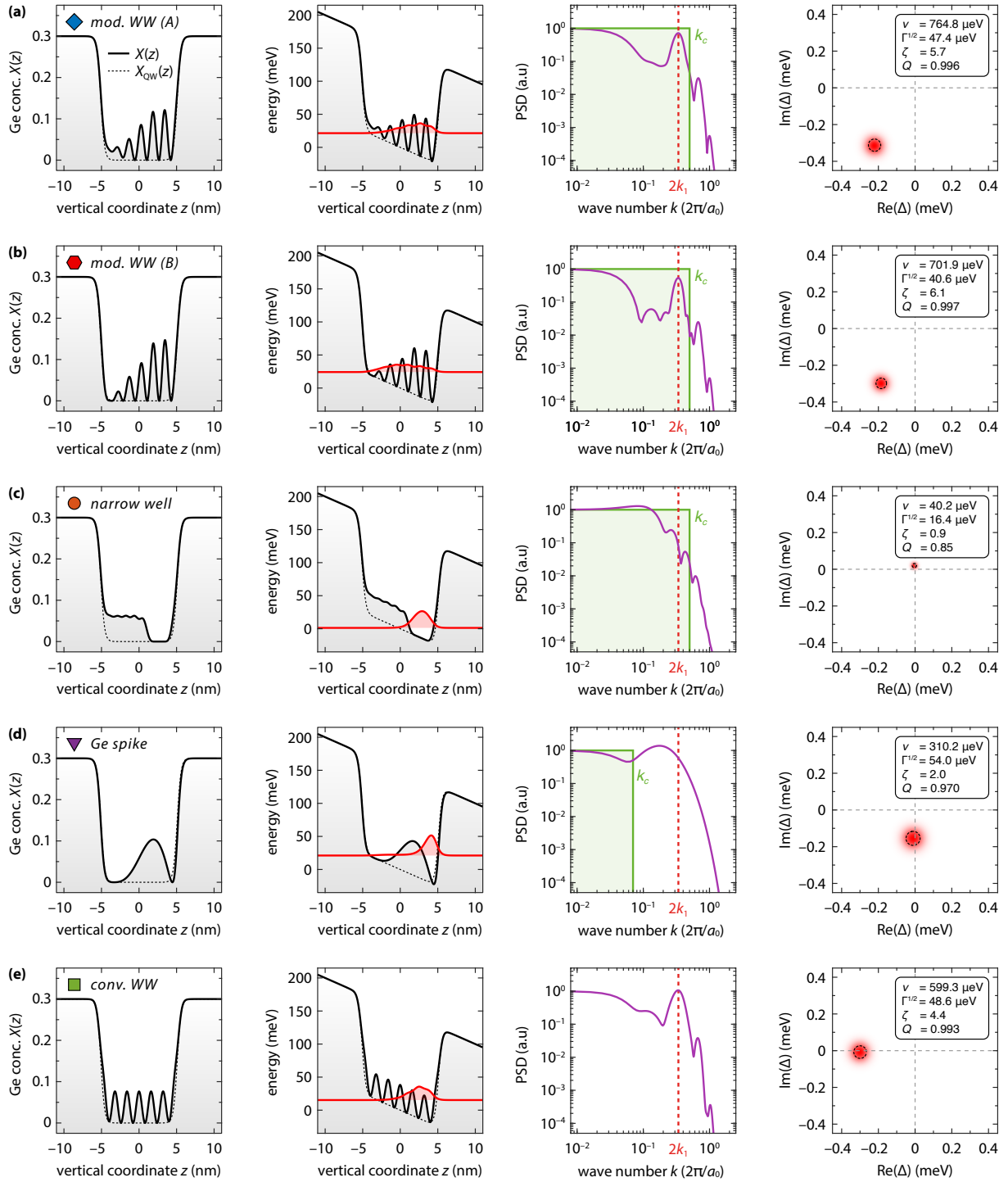


**Fig. 2.** Optimization results for a fixed Ge budget  $x_{\text{Ge}} = 5\%$  distributed within the QW. **(a)** Optimization with the cost functional  $J_0^{(A)}$  (maximum deterministic component) at a cutoff wave number  $k_c = 0.5 \times 2\pi/a_0$  yield a modulated wiggles well. **(b)** A similar structure is found when optimizing with the cost functional  $J_0^{(B)}$  (reliable enhancement) at the same cutoff wave number. **(c)** Optimization with the cost functional  $J_0^{(C)}$  (minimum random component) at the same  $k_c$  yields a narrow well. **(d)** Epitaxial profile with a Ge spike obtained by maximizing the deterministic component (with cost functional  $J_0^{(A)}$ ) at a reduced cutoff wave number  $k_c = 0.07 \times 2\pi/a_0$ . **(e)** Conventional wiggles well with wave number  $2k_1$  for comparison. In all plots, the first column shows the epitaxial Ge profile and the second column is the potential energy and ground state envelope wave function at  $F = 5 \text{ mV/nm}$ . The third column shows the power spectral density (PSD) of the function  $S(z)$ , see Eq. (32), and the fourth column illustrates shows the statistical distribution of the intervalley coupling parameter  $\Delta$  in the complex plane.

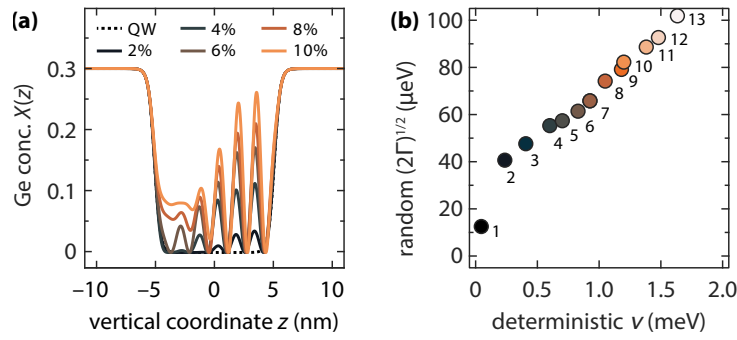


**Fig. 3.** Modulated wiggles optimizing the reliable enhancement (B) for different total Ge concentrations  $x_{\text{Ge}}$  in the QW. **(a)** Optimized epitaxial profiles for different Ge budgets  $x_{\text{Ge}} = \{2\%, 4\%, 6\%, 8\%, 10\%\}$ . **(b)** Deterministic  $\nu$  and disorder-induced contributions  $\sqrt{2\Gamma}$  to the intervalley coupling parameter for the modulated wiggles optimized at different Ge concentrations. The labels indicate the respective Ge concentration in percent.

We have repeated the optimization for the objective (B) for different total Ge budgets in the QW domain. The results shown in Fig. 3 (a) are variants of the modulated wiggles with increasing Ge amplitudes for large Ge budgets, in particular close to the upper interface. All modulated wiggles computed via the optimization procedure show a monotonic increase of both the deterministic and disorder-induced contributions to the intervalley coupling parameter for growing Ge content as shown in Fig. 3 (b). We emphasize that higher Ge concentrations also increase the spin-orbit interaction strength [67], which has not been taken into account in the present study.

The modulated wiggles offer a great range of tunability of the valley splitting via the vertical electric field. Fig. 4 (a) shows the mean valley splitting  $\langle E_{\text{VS}} \rangle$  for electrons in a modulated wiggles (B) with  $x_{\text{Ge}} = 5\%$  optimized at  $F = 5 \text{ mV/nm}$  and a conventional  $2k_1$  wiggles with the same overall Ge content as a function of the applied electric field  $F$ . While the mean valley splitting in a conventional wiggles is only weakly dependent on the electric field, the opposite is true for the modulated wiggles. We observe a wide range of tunability from  $\langle E_{\text{VS}} \rangle \approx 200 \mu\text{eV}$  (for  $F$  large negative) to  $\langle E_{\text{VS}} \rangle > 1 \text{ meV}$  (for  $F$  large positive). The point of maximum sensitivity is near the design field strength  $F_{\text{opt}}$ , see Fig. 4 (b). This pronounced field dependency is explained by the different confinement behavior of the electronic wave function shown in Fig. 4 (c). At large negative  $F$ , the envelope wave function does not probe the Ge-rich modulations, such that the structure effectively behaves like a conventional Si/SiGe QW with smooth interfaces. In the opposite case, at large positive field strength, the envelope overlaps dominantly with the most Ge-rich segments only, leading to a large valley splitting expectation value. Over the entire range of electric fields, the deterministic component dominates over the disorder-induced contribution to the valley splitting. We believe that this enhanced tunability could be useful to switch from high to low valley splitting regimes on demand, *e.g.*, in order to control the rate of phonon-assisted valley relaxation [22, 52, 54] to ensure a definite valley state prior to the execution of two-qubit gates. Moreover, the modulated wiggles design could be relevant for the tuning of energy splittings of hybrid qubits [68, 69]. To achieve a wide-range tunability of the electric field, advanced device designs with back gate electrodes are advantageous [45].

## 4.2 Narrow Well

When optimizing for the reduction of the disorder-induced component (C), we obtain the epitaxial profile shown in Fig. 2 (c). The second column shows the envelope wave function of the ground state electron, which makes clear how the reduction of disorder is achieved: By accumulating the Ge atoms in a plateau near the bottom QW interface, the structure becomes effectively a narrow QW, where the

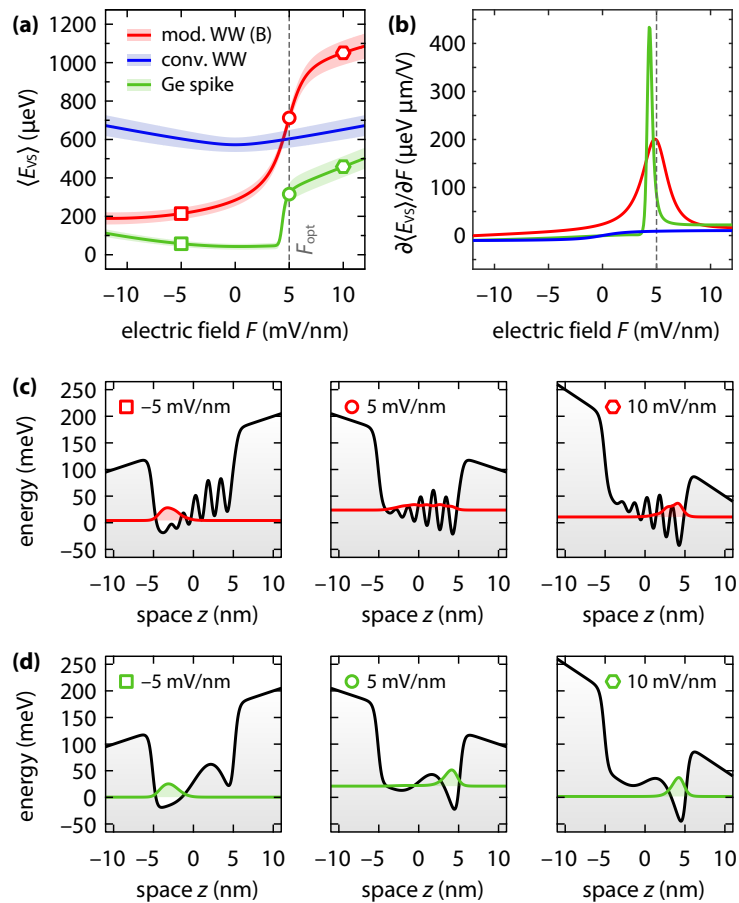


**Fig. 4.** (a) Mean valley splitting  $\langle E_{VS} \rangle$  of the modulated wiggles (red), the Ge spike (green) and the conventional long-period wiggles (blue) as a function of the applied electric field  $F$ . All structures contain in total 5% Ge in the QW domain. Due to the asymmetry in their epitaxial profiles, the modulated wiggles and the Ge spike exhibit a strong, non-symmetric field dependency, which allows for tuning into a high and low valley splitting regime. For comparison, the field dependency of the conventional wiggles is only weak and fully symmetric under inversion of the field strength  $F \leftrightarrow -F$ . The shaded regions indicate the [25%, 75%] percentile of the Rice distribution (16). (b) Sensitivity of the mean valley splitting on the electric field  $\partial \langle E_{VS} \rangle / \partial F$  as a function of the applied electric field. The field sensitivity of two non-symmetric structures is peaked around the design field strength  $F_{opt}$ . In contrast, the conventional wiggles show only a weak field dependency. (c) Cross section of the total potential energy landscape and the electronic ground state envelope wave function for the modulated wiggles at different electric fields. (d) Same cross sections for the Ge spike. The localization of the envelope wave function is strongly dependent on the electric field such that different parts of the non-symmetric epitaxial profiles are probed in the low and high valley splitting regimes.

electron is localized in a narrow Ge-free segment. In combination with additional smoothing of the upper interface, this leads to a reduction of the overlap with Ge atoms and therefore to a reduction of valley splitting volatility (see also the complex plane distribution in the fourth column). The narrow well provides only a weak deterministic valley splitting, such that the deterministic component ratio is small ( $Q = 0.85$ ,  $\zeta = 0.9$ ).

### 4.3 Germanium Spike

We return to the maximization of the deterministic component (A), but with a reduced cutoff wave number  $k_c = 0.07 \times 2\pi/a_0$  in order to suppress the  $2k_1$  resonance. In this case, our optimization procedure yields a single Ge peak at about 3 nm below the upper interface, see Fig. 2 (d). The structure allows for a significant deterministic enhancement due to a higher order effect, where the combination

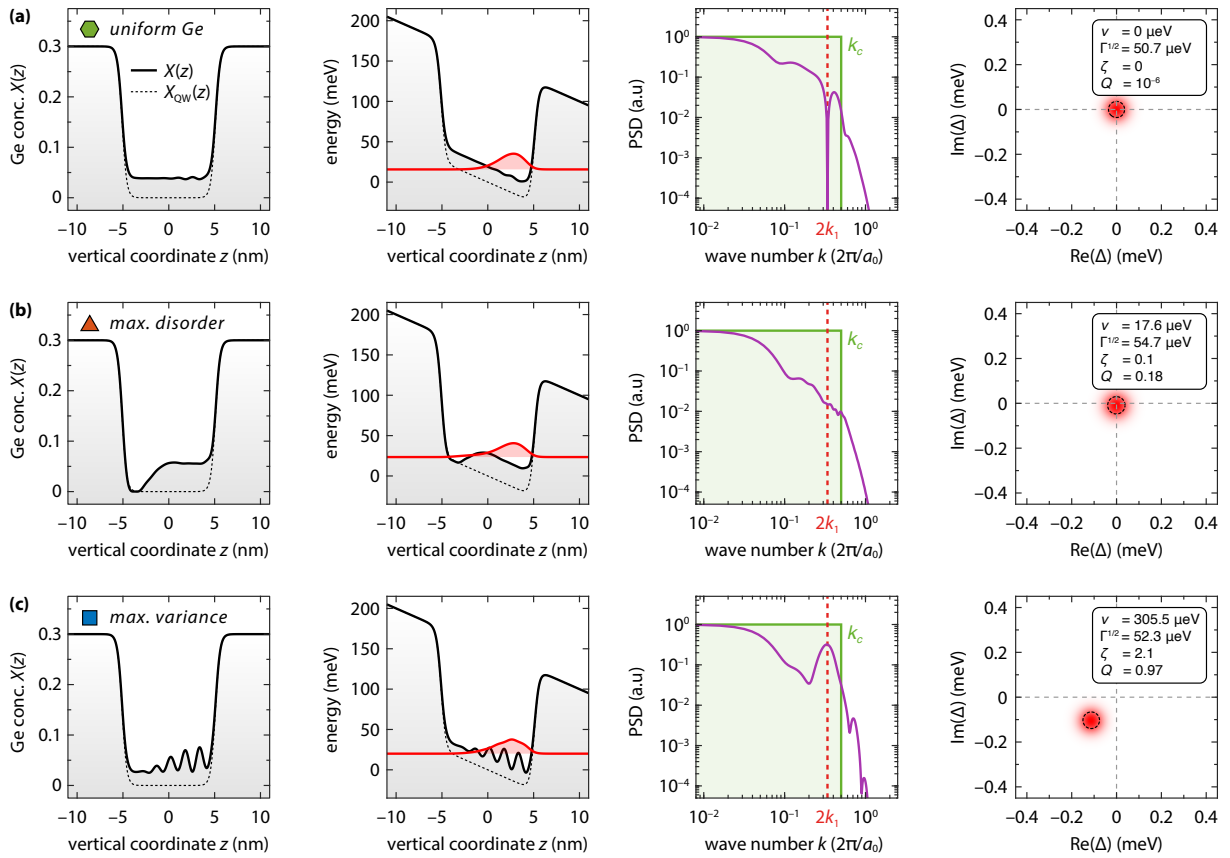


**Fig. 5.** Optimization under inverted objectives. **(a)** Minimization of the deterministic component (D) leads to a (nearly) uniform Ge distribution in the QW. The PSD (third column) shows a sharp dropout around  $2k_1$ , such that the resulting valley splitting is fully disorder-induced. **(b)** Maximization of the disorder-induced component (E) of the intervalley coupling parameter yields a profile similar to the uniform Ge distribution, but with an increased Ge content in the region that overlaps with the envelope wave function. **(c)** Maximization of the valley splitting variance (F) leads to a wiggly-well type structure with non-zero baseline Ge concentration.

of the heterostructure potential and the envelope wave function boosts the  $2k_1$ -resonance (see the PSD in the third column). On the other hand, the strong overlap with Ge-rich domains leads to a large disorder-induced component, too. More details on the underlying mechanism are given in Ref. [44]. We remark that the structure has some similarity with the “Ge spike” described in Refs. [34, 35, 40], which is why we adopt this notion here. Finally, the valley splitting in the Ge spike has a similar field tunability as the modulated wiggly well, but with a smaller range of achievable mean valley splittings, see Fig. 4 (a)–(b). The underlying mechanism is shown in Fig. 4 (c), which corresponds to a tunable double dot system with strongly different confinement potentials near the top and bottom interface.

#### 4.4 Optimization of Inverted Objectives

It is illustrative to carry out the epitaxial profile optimization also under inversion of the objective functions to investigate solutions that enhance undesirable properties. Specifically, we consider optimization objectives inverse to  $J_0^{(A)}(x, \psi_0)$  and  $J_0^{(C)}(x, \psi_0)$  to obtain structures with either very low deterministic or highly volatile valley splittings. In addition, we investigate the maximization of the variance of the valley splitting (spread of the Rice distribution), see Eq. (18). We consider:

(D) Minimization of deterministic component

$$J_0^{(D)}(x, \psi_0) = \frac{1}{J_0^{(A)}(x, \psi_0)} = \frac{\nu(x, \psi_0)}{E_{\text{ref}}}.$$

(E) Maximization of disorder-induced random component

$$J_0^{(E)}(x, \psi_0) = \frac{1}{J_0^{(C)}(x, \psi_0)} = \frac{E_{\text{ref}}}{\sqrt{2\Gamma(x, \psi_0)}}.$$

(F) Maximization of the valley splitting variance

$$J_0^{(F)}(x, \psi_0) = \frac{E_{\text{ref}}}{\sqrt{\text{Var}(E_{\text{VS}}(x, \psi_0))}}.$$

The numerical results for a limited Ge budget  $x_{\text{Ge}} = 5\%$  and cutoff wave number  $k_c = 0.5 \times 2\pi/a_0$  are shown in Fig. 5.

For the minimization of the deterministic component (D) we obtain a (nearly) uniform Ge concentration in the QW, see Fig. 5(a). The combination of the confinement potential and the envelope wave function leads to a PSD that features a sharp dropout around wave number  $2k_1$ , such that contributions to the deterministic enhancement of the valley splitting are strongly suppressed. The valley splitting is thus *fully* disorder-induced and has no deterministic enhancement at all. While the uniform Ge concentration leads to an enhancement of the mean valley splitting in comparison to the pure silicon QW (with the same interface width), this enhancement comes along with a large volatility. As a consequence, numerous spin-valley hotspots are to be expected in these structures. Quantum wells with uniform Ge concentration profiles have been studied in Refs. [30, 40, 52].

The maximization of the disorder-induced random component (E) leads to an epitaxial structure similar to the uniform Ge distribution, but with an enhanced Ge accumulation in the region that overlaps with the envelope wave function, see Fig. 5(b). In order to respect the limited Ge budget constraint, the Ge concentration is reduced near the lower interface to provide additional Ge atoms in the overlap region with the electronic envelope wave function. The epitaxial structure is similar to a mirror inverse of the narrow well profile shown in Fig. 2(c), which is interesting as the optimization objective  $J_0^{(E)}$  is the inverse of  $J_0^{(C)}$ . The magnitude of the disorder-induced component is, however, only slightly larger than in case (D) or the Ge spike in Fig. 2(d).

Finally, we consider maximization of the valley splitting variance (F), which differs from maximization of the disorder-induced component as the spread of the Rice distribution can become larger at higher mean values. The result is shown in Fig. 5(c), which is a wigggle-well type profile but with non-zero baseline Ge concentration. As in cases (A) and (B), the wigggle well structure induces a vertically stretched envelope wave function that is extended over almost the entire QW domain. This way, a large overlap with disorder-inducing Ge atoms is achieved, leading to a large variance of the valley splitting. The magnitude of the deterministic and disorder-induced components are very similar to that of the Ge spike, see Fig. 6, which underpins again the large uncertainty of the valley splitting in the Ge spike heterostructure.

## 5 Summary and Conclusion

We have developed a variational optimization approach for the computation of Ge concentration profiles in Si/SiGe QWs to enhance the valley splitting in gate-defined QDs. We investigated a number of

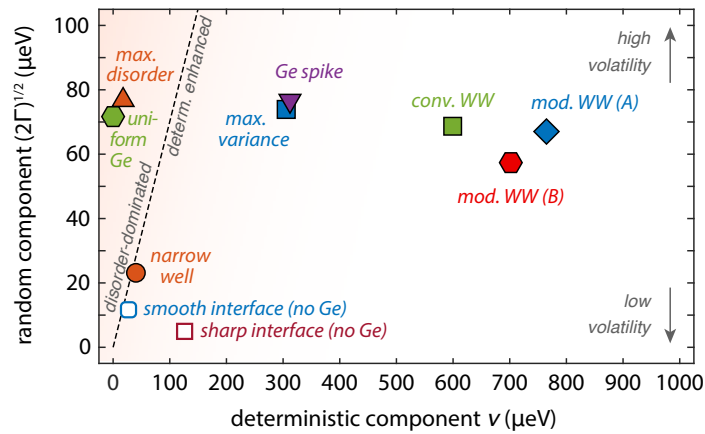


**Fig. 6.** Comparison of deterministic and disorder-induced components for the different heterostructures obtained by variational optimization with limited Ge budget  $x_{\text{Ge}} = 5\%$ . The dashed line indicates  $\nu/\sqrt{2\Gamma} = 0.3507$ , which separates the disorder-dominated from the deterministically enhanced regime ( $Q = 0.5$ ). For comparison, the plot shows also the values of a smooth ( $\sigma_{u,l} = 0.5$  nm) and a sharp ( $\sigma_{u,l} = 0$  nm) interface with no Ge included in the QW.

different optimization objectives, including maximization of the deterministic component, minimization of the disorder-induced component and optimal balancing of both contributions (reliable enhancement). Our method has recovered heuristic heterostructure designs previously described in the literature as special solutions of a constrained optimization problem (e.g., wiggles, Ge spike, narrow well, uniform Ge concentration). The characteristics of the various profiles are summarized in Fig. 6, which shows the typical deterministic and disorder-induced contributions to the valley splitting expected for the structures with a total Ge content of 5% in the QW domain. For comparison, the plot also shows the results for conventional  $\text{Si}_{0.7}\text{Ge}_{0.3}/\text{Si}/\text{Si}_{0.7}\text{Ge}_{0.3}$  QWs (with no Ge in the QW domain) with smooth and sharp interfaces. The results of the optimization objectives (A) and (B) are far in the deterministically enhanced regime, while the result of (C) offers only a weak deterministic enhancement. The optimization for the inverted objectives (D) and (E) leads to structures deep inside the disorder-dominated regime.

Our main result is the *modulated wiggles*, that is a modification of the conventional sinusoidal wiggles profile, which is adapted to the local field gradient. We have shown that the modulated wiggles well outperforms the conventional wiggles well by offering both a larger deterministic component and a reduced disorder-related contribution to the intervalley coupling parameter (i.e., it provides a more reliable enhancement), see Fig. 6. These properties are crucial to ensure a high degree of reproducibility of qubits across devices required for a scalable quantum computing technology platform. Moreover, the modulated wiggles well shows a strong dependency on the applied electric field, which allows for a wide-range tunability of the mean valley splitting from  $200 \mu\text{eV}$  to more than  $1 \text{ meV}$ . We believe that these enhanced prospects for tunability can be useful for the design of *switchable* spin qubits with on-demand adjustable valley splitting, e.g., to control the rate of relaxation processes prior to quantum gate operations or readout.

## A Mean, Covariance and Pseudo-Covariance

Following [44], we employ a factorization ansatz for the ground state envelope wave function

$$\Psi_0(\mathbf{r}) = \phi_0(x, y) \psi_0(z)$$

separating the problem in vertical and in-plane directions. The expressions for the deterministic valley splitting (14) and the covariance and pseudo-covariance (15) are evaluated using the ground state

wave function of the two-dimensional QD

$$\phi_0(x, y) = \frac{1}{\pi^{1/4} l_x^{1/2}} e^{-\frac{1}{2}(x/l_x)^2} \times \frac{1}{\pi^{1/4} l_y^{1/2}} e^{-\frac{1}{2}(y/l_y)^2}$$

where  $l_i^2 = \hbar / (m_i \omega_i)$ ,  $i \in \{x, y\}$ . With this, we derive expressions for the deterministic component

$$\begin{aligned} \Delta_{\text{det}}(x, \psi_0) &= \sum_n C_n^{(2)} e^{-\left(\frac{nG_0 x l_x}{2}\right)^2} e^{-\left(\frac{nG_0 y l_y}{2}\right)^2} \times \\ &\int dz e^{-i(nG_0 z + 2k_0)z} \left( U_{\text{QW}}(z) + U_F(z) + \right. \\ &\left. + \frac{\hbar\omega_x}{2} \left[ \frac{1}{2} - \left( \frac{nG_0 x l_x}{2} \right)^2 \right] + \frac{\hbar\omega_y}{2} \left[ \frac{1}{2} - \left( \frac{nG_0 y l_y}{2} \right)^2 \right] \right) \psi_0^2(z) \end{aligned} \quad (33)$$

and the covariance

$$\begin{aligned} \Gamma(x, \psi_0) &= \frac{(\Delta E_c)^2 \Omega_a}{2\pi l_x l_y} \sum_n C_n^{(4)} e^{-\left(\frac{nG_0 x l_x}{\sqrt{2}2}\right)^2} e^{-\left(\frac{nG_0 y l_y}{\sqrt{2}2}\right)^2} \\ &\times \int dz e^{-inG_0 z} X(z) (1 - X(z)) \psi_0^4(z). \end{aligned}$$

The pseudo covariance is obtained as

$$\begin{aligned} C(x, \psi_0) &= \frac{(\Delta E_c)^2 \Omega_a}{2\pi l_x l_y} \sum_n D_n^{(4)} e^{-\left(\frac{nG_0 y l_y}{2\sqrt{2}}\right)^2} e^{-\left(\frac{nG_0 x l_x}{2\sqrt{2}}\right)^2} \\ &\times \int dz e^{-i(nG_0 z + 4k_0)z} X(z) (1 - X(z)) \psi_0^4(z). \end{aligned}$$

The Bloch factor coefficients in the above equations are

$$C_n^{(2)} = \sum_{\mathbf{G}, \mathbf{G}'} c_+^*(\mathbf{G}) c_-(\mathbf{G}') \delta_{\mathbf{G}-\mathbf{G}', n\mathbf{G}_0}$$

with

$$\mathbf{G}_0 = (I - \varepsilon) (\mathbf{b}_1 + \mathbf{b}_2) = \frac{4\pi}{a_0} \begin{pmatrix} -\varepsilon_{z,x} \\ -\varepsilon_{y,z} \\ 1 - \varepsilon_{z,z} \end{pmatrix}.$$

The coefficients for the covariance and pseudo-covariance are obtained from the set of  $C_n^{(2)}$  coefficients as

$$\begin{aligned} C_n^{(4)} &= \sum_m C_{m-n}^{(2)*} C_m^{(2)}, \\ D_n^{(4)} &= \sum_m C_m^{(2)} C_{n-m}^{(2)}. \end{aligned}$$

Due to the rapidly oscillating factor  $\exp(-4ik_0 z)$  in the integrand, the pseudo-covariance is typically much smaller than the covariance  $|C| \ll \Gamma$ . Hence, the pseudo-covariance is ignored in most of the computations by employing the circular approximation, see Sec. 2.3.

## B Conventional Wiggle Well

The free-shape optimization results are compared with the conventional sinusoidal (long-period) wiggle well given as

$$x_{\text{ww}}(z) = A \sin^2(k_1 z) \Xi(z),$$

where  $A$  is the Ge concentration amplitude. The indicator function  $\Xi(z)$  restricts the wiggle well to the QW domain. For a fair comparison, we choose the amplitude  $A$  such that the overall Ge concentration matches the target Ge budget. Hence, the amplitude is chosen such that it holds

$$\overline{X}(x_{\text{ww}}(A)) - x_{\text{Ge}} = 0.$$

The function to quantify the mean Ge content  $\overline{X}(x)$  of a particular profile is given in Eq. (22). The equation is solved for  $A$  numerically. For  $x_{\text{Ge}} = 5\%$  in a  $h = 75$  ML QW we obtain  $A = 0.0764$ .

## References

- [1] F. A. Zwanenburg, A. S. Dzurak, A. Morello, M. Y. Simmons, L. C. L. Hollenberg, G. Klimeck, S. Rogge, S. N. Coppersmith, and M. A. Eriksson, "Silicon quantum electronics", *Rev. Mod. Phys.* **85**, 961–1019 (2013) DOI: [10.1103/RevModPhys.85.961](https://doi.org/10.1103/RevModPhys.85.961).
- [2] G. Burkard, T. D. Ladd, A. Pan, J. M. Nichol, and J. R. Petta, "Semiconductor spin qubits", *Rev. Mod. Phys.* **95**, 025003 (2023) DOI: [10.1103/RevModPhys.95.025003](https://doi.org/10.1103/RevModPhys.95.025003).
- [3] G. Hu, W. W. Huang, R. Cai, L. Wang, C. H. Yang, G. Cao, X. Xue, P. Huang, and Y. He, "Single-electron spin qubits in silicon for quantum computing", *Intell. Comput.* **4**, 0115 (2025) DOI: [10.34133/icomputing.0115](https://doi.org/10.34133/icomputing.0115).
- [4] A. M. Tyryshkin, S. Tojo, J. J. L. Morton, H. Riemann, N. V. Abrosimov, P. Becker, H.-J. Pohl, T. Schenkel, M. L. W. Thewalt, K. M. Itoh, and S. A. Lyon, "Electron spin coherence exceeding seconds in high-purity silicon", *Nat. Mater.* **11**, 143–147 (2011) DOI: [10.1038/nmat3182](https://doi.org/10.1038/nmat3182).
- [5] Y. Song, J. Yun, J. Kim, W. Jang, H. Jang, J. Park, M.-K. Cho, H. Sohn, N. Usami, S. Miyamoto, K. M. Itoh, and D. Kim, "Coherence of a field gradient driven singlet-triplet qubit coupled to multielectron spin states in  $^{28}\text{Si}/\text{SiGe}$ ", *npj Quantum Inf.* **10**, 77 (2024) DOI: [10.1038/s41534-024-00869-y](https://doi.org/10.1038/s41534-024-00869-y).
- [6] P. Daoust, N. Rotaru, D. Biswas, S. Koelling, E. Rahier, A. Dubé-Valade, P. Del Vecchio, M. S. Edwards, M. Tanvir, E. Sajadi, J. Salfi, and O. Moutanabbir, "Nuclear spin-free  $^{70}\text{Ge}/^{28}\text{Si}^{70}\text{Ge}$  quantum well heterostructures grown on industrial SiGe-buffered wafers", (2025) DOI: [10.48550/arXiv.2511.01916](https://doi.org/10.48550/arXiv.2511.01916).
- [7] H. C. George et al., "12-spin-qubit arrays fabricated on a 300 mm semiconductor manufacturing line", *Nano Letters* **25**, 793–799 (2025) DOI: [10.1021/acs.nanolett.4c05205](https://doi.org/10.1021/acs.nanolett.4c05205).
- [8] T. Huckemann, P. Muster, W. Langheinrich, V. Brackmann, M. Friedrich, N. D. Komerički, L. K. Diebel, V. Stieß, D. Bougeard, C. Dahl, L. R. Schreiber, and H. Bluhm, "Industrially fabricated single-electron quantum dots in Si/Si-Ge heterostructures", *IEEE Electron Device Lett.* **46**, 868–871 (2025) DOI: [10.1109/LED.2025.3553672](https://doi.org/10.1109/LED.2025.3553672).
- [9] S. Neyens et al., "Probing single electrons across 300-mm spin qubit wafers", *Nature* **629**, 80–85 (2024) DOI: [10.1038/s41586-024-07275-6](https://doi.org/10.1038/s41586-024-07275-6).
- [10] T. Koch, C. Godfrin, V. Adam, J. Ferrero, D. Schroller, N. Glaeser, S. Kubicek, R. Li, R. Loo, S. Massar, G. Simion, D. Wan, K. De Greve, and W. Wernsdorfer, "Industrial 300 mm wafer processed spin qubits in natural silicon/silicon-germanium", *npj Quantum Inf.* **11**, 59 (2025) DOI: [10.1038/s41534-025-01016-x](https://doi.org/10.1038/s41534-025-01016-x).
- [11] J. Yoneda, K. Takeda, T. Otsuka, T. Nakajima, M. R. Delbecq, G. Allison, T. Honda, T. Kodera, S. Oda, Y. Hoshi, N. Usami, K. M. Itoh, and S. Tarucha, "A quantum-dot spin qubit with coherence limited by charge noise and fidelity higher than 99.9%", *Nat. Nanotechnol.* **13**, 102–106 (2017) DOI: [10.1038/s41565-017-0014-x](https://doi.org/10.1038/s41565-017-0014-x).
- [12] D. M. Zajac, A. J. Sigillito, M. Russ, F. Borjans, J. M. Taylor, G. Burkard, and J. R. Petta, "Resonantly driven CNOT gate for electron spins", *Science* **359**, 439–442 (2018) DOI: [10.1126/science.aao5965](https://doi.org/10.1126/science.aao5965).
- [13] A. Noiri, K. Takeda, T. Nakajima, T. Kobayashi, A. Sammak, G. Scappucci, and S. Tarucha, "Fast universal quantum gate above the fault-tolerance threshold in silicon", *Nature* **601**, 338–342 (2022) DOI: [10.1038/s41586-021-04182-y](https://doi.org/10.1038/s41586-021-04182-y).
- [14] X. Xue, M. Russ, N. Samkharadze, B. Undseth, A. Sammak, G. Scappucci, and L. M. K. Vandersypen, "Quantum logic with spin qubits crossing the surface code threshold", *Nature* **601**, 343–347 (2022) DOI: [10.1038/s41586-021-04273-w](https://doi.org/10.1038/s41586-021-04273-w).

- [15] S. G. J. Philips, M. T. Mađzik, S. V. Amitonov, S. L. de Snoo, M. Russ, N. Kalhor, C. Volk, W. I. L. Lawrie, D. Brousse, L. Tryputen, B. P. Wuetz, A. Sammak, M. Veldhorst, G. Scappucci, and L. M. K. Vandersypen, “Universal control of a six-qubit quantum processor in silicon”, *Nature* **609**, 919–924 (2022) DOI: [10.1038/s41586-022-05117-x](https://doi.org/10.1038/s41586-022-05117-x).
- [16] A. R. Mills, C. R. Guinn, M. J. Gullans, A. J. Sigillito, M. M. Feldman, E. Nielsen, and J. R. Petta, “Two-qubit silicon quantum processor with operation fidelity exceeding 99%”, *Sci. Adv.* **8**, eabn5130 (2022) DOI: [10.1126/sciadv.abn5130](https://doi.org/10.1126/sciadv.abn5130).
- [17] Y.-H. Wu, L. C. Camenzind, P. Büttler, I. K. Jin, A. Noiri, K. Takeda, T. Nakajima, T. Kobayashi, G. Scappucci, H.-S. Goan, and S. Tarucha, “Simultaneous high-fidelity single-qubit gates in a spin qubit array”, (2025) DOI: [10.48550/arXiv.2507.11918](https://doi.org/10.48550/arXiv.2507.11918).
- [18] I. F. de Fuentes, E. Raymenants, B. Undseth, O. Pietx-Casas, S. P. M. Mađzik, S. L. de Snoo, S. V. Amitonov, L. Tryputen, A. T. Schmitz, A. Y. Matsuura, G. Scappucci, and L. M. K. Vandersypen, “Running a six-qubit quantum circuit on a silicon spin qubit array”, (2025) DOI: [10.48550/arXiv.2505.19200](https://doi.org/10.48550/arXiv.2505.19200).
- [19] H. Sohn, J. Jung, J. Park, H. Jang, L. E. A. Stehouwer, D. Degli Esposti, G. Scappucci, and D. Kim, “Application of zero-noise-extrapolation-based quantum error mitigation to a silicon spin qubit”, *Phys. Rev. A* **112** (2025) DOI: [10.1103/925y-b4s1](https://doi.org/10.1103/925y-b4s1).
- [20] K. Takeda, A. Noiri, T. Nakajima, T. Kobayashi, and S. Tarucha, “Quantum error correction with silicon spin qubits”, *Nature* **608**, 682–686 (2022) DOI: [10.1038/s41586-022-04986-6](https://doi.org/10.1038/s41586-022-04986-6).
- [21] L. M. K. Vandersypen, H. Bluhm, J. S. Clarke, A. S. Dzurak, R. Ishihara, A. Morello, D. J. Reilly, L. R. Schreiber, and M. Veldhorst, “Interfacing spin qubits in quantum dots and donors—hot, dense, and coherent”, *npj Quantum Inf.* **3**, 34 (2017) DOI: [10.1038/s41534-017-0038-y](https://doi.org/10.1038/s41534-017-0038-y).
- [22] V. Langrock, J. A. Krzywda, N. Focke, I. Seidler, L. R. Schreiber, and Ł. Cywiński, “Blueprint of a scalable spin qubit shuttle device for coherent mid-range qubit transfer in disordered Si/SiGe/SiO<sub>2</sub>”, *PRX Quantum* **4**, 020305 (2023) DOI: [10.1103/PRXQuantum.4.020305](https://doi.org/10.1103/PRXQuantum.4.020305).
- [23] M. Künne, A. Willmes, M. Oberländer, C. Gorjaew, J. D. Teske, H. Bhardwaj, M. Beer, E. Kammerloher, R. Otten, I. Seidler, R. Xue, L. R. Schreiber, and H. Bluhm, “The SpinBus architecture for scaling spin qubits with electron shuttling”, *Nat. Commun.* **15**, 4977 (2024) DOI: [10.1038/s41467-024-49182-4](https://doi.org/10.1038/s41467-024-49182-4).
- [24] F. Ginzler, M. Fellner, C. Ertler, L. R. Schreiber, H. Bluhm, and W. Lechner, “Scalable parity architecture with a shuttling-based spin qubit processor”, *Phys. Rev. B* **110**, 075302 (2024) DOI: [10.1103/PhysRevB.110.075302](https://doi.org/10.1103/PhysRevB.110.075302).
- [25] I. Seidler, T. Struck, R. Xue, N. Focke, S. Trellenkamp, H. Bluhm, and L. R. Schreiber, “Conveyor-mode single-electron shuttling in Si/SiGe for a scalable quantum computing architecture”, *npj Quantum Inf.* **8**, 100 (2022) DOI: [10.1038/s41534-022-00615-2](https://doi.org/10.1038/s41534-022-00615-2).
- [26] R. Xue, M. Beer, I. Seidler, S. Humpohl, J.-S. Tu, S. Trellenkamp, T. Struck, H. Bluhm, and L. R. Schreiber, “Si/SiGe qubus for single electron information-processing devices with memory and micron-scale connectivity function”, *Nat. Commun.* **15**, 2296 (2024) DOI: [10.1038/s41467-024-46519-x](https://doi.org/10.1038/s41467-024-46519-x).
- [27] T. Struck, M. Volmer, L. Visser, T. Offermann, R. Xue, J.-S. Tu, S. Trellenkamp, Ł. Cywiński, H. Bluhm, and L. R. Schreiber, “Spin-epr-pair separation by conveyor-mode single electron shuttling in Si/SiGe”, *Nat. Commun.* **15**, 1325 (2024) DOI: [10.1038/s41467-024-45583-7](https://doi.org/10.1038/s41467-024-45583-7).
- [28] M. De Smet, Y. Matsumoto, A.-M. J. Zwerver, L. Tryputen, S. L. de Snoo, S. V. Amitonov, S. R. Katirae-Far, A. Sammak, N. Samkharadze, Ö. Gül, R. N. M. Wasserman, E. Greplová, M. Rimbach-Russ, G. Scappucci, and L. M. K. Vandersypen, “High-fidelity single-spin shuttling in silicon”, *Nat. Nanotechnol.* **20**, 866–872 (2025) DOI: [10.1038/s41565-025-01920-5](https://doi.org/10.1038/s41565-025-01920-5).
- [29] J. Klos, J. Tröger, J. Keutgen, M. P. Losert, N. V. Abrosimov, J. Knoch, H. Bracht, S. N. Coppersmith, M. Friesen, O. Cojocaru-Mirédin, L. R. Schreiber, and D. Bougeard, “Atomistic compositional details and their importance for spin qubits in isotope-purified silicon quantum wells”, *Adv. Sci.* **11**, 2407442 (2024) DOI: [10.1002/advs.202407442](https://doi.org/10.1002/advs.202407442).
- [30] B. Paquelet Wuetz, M. P. Losert, S. Koelling, L. E. A. Stehouwer, A.-M. J. Zwerver, S. G. J. Philips, M. T. Mađzik, X. Xue, G. Zheng, M. Lodari, S. V. Amitonov, N. Samkharadze, A. Sammak, L. M. K. Vandersypen, R. Rahman, S. N. Coppersmith, O. Moutanabbir, M. Friesen, and G. Scappucci, “Atomic fluctuations lifting the energy degeneracy in Si/SiGe quantum dots”, *Nat. Commun.* **13**, 7730 (2022) DOI: [10.1038/s41467-022-35458-0](https://doi.org/10.1038/s41467-022-35458-0).
- [31] J. P. Dodson, H. E. Ercan, J. Corrigan, M. P. Losert, N. Holman, T. McJunkin, L. F. Edge, M. Friesen, S. N. Coppersmith, and M. A. Eriksson, “How valley-orbit states in silicon quantum dots probe quantum well interfaces”, *Phys. Rev. Lett.* **128**, 146802 (2022) DOI: [10.1103/PhysRevLett.128.146802](https://doi.org/10.1103/PhysRevLett.128.146802).
- [32] D. Degli Esposti, L. E. A. Stehouwer, O. Gül, N. Samkharadze, C. Déprez, M. Meyer, I. N. Meijer, L. Tryputen, S. Karwal, M. Botifoll, J. Arbiol, S. V. Amitonov, L. M. K. Vandersypen, A. Sammak, M. Veldhorst, and G. Scappucci, “Low disorder and high valley splitting in silicon”, *npj Quantum Inf.* **10**, 32 (2024) DOI: [10.1038/s41534-024-00826-9](https://doi.org/10.1038/s41534-024-00826-9).

- [33] M. Volmer, T. Struck, J.-S. Tu, S. Trellenkamp, D. D. Esposti, G. Scappucci, Ł. Cywiński, H. Bluhm, and L. R. Schreiber, “Reduction of the impact of the local valley splitting on the coherence of conveyor-belt spin shuttling in  $^{28}\text{Si/SiGe}$ ”, (2025) DOI: [10.48550/arXiv.2510.03773](https://doi.org/10.48550/arXiv.2510.03773).
- [34] T. McJunkin, E. R. MacQuarrie, L. Tom, S. F. Neyens, J. P. Dodson, B. Thorgrimsson, J. Corrigan, H. E. Ercan, D. E. Savage, M. G. Lagally, R. Joynt, S. N. Coppersmith, M. Friesen, and M. A. Eriksson, “Valley splittings in Si/SiGe quantum dots with a germanium spike in the silicon well”, *Phys. Rev. B* **104**, 085406 (2021) DOI: [10.1103/PhysRevB.104.085406](https://doi.org/10.1103/PhysRevB.104.085406).
- [35] T. Salamone, B. M. Diaz, J. Li, L. Cvitkovich, and Y.-M. Niquet, “Valley physics in the two bands k.p model for SiGe heterostructures and spin qubits”, (2025) DOI: [10.48550/arXiv.2511.20153](https://doi.org/10.48550/arXiv.2511.20153).
- [36] L. Zhang, J.-W. Luo, A. Saraiva, B. Koiller, and A. Zunger, “Genetic design of enhanced valley splitting towards a spin qubit in silicon”, *Nat. Commun.* **4**, 2396 (2013) DOI: [10.1038/ncomms3396](https://doi.org/10.1038/ncomms3396).
- [37] G. Wang, Z.-G. Song, J.-W. Luo, and S.-S. Li, “Origin of giant valley splitting in silicon quantum wells induced by superlattice barriers”, *Phys. Rev. B* **105**, 165308 (2022) DOI: [10.1103/PhysRevB.105.165308](https://doi.org/10.1103/PhysRevB.105.165308).
- [38] T. McJunkin, B. Harpt, Y. Feng, M. P. Losert, R. Rahman, J. P. Dodson, M. A. Wolfe, D. E. Savage, M. G. Lagally, S. N. Coppersmith, M. Friesen, R. Joynt, and M. A. Eriksson, “SiGe quantum wells with oscillating Ge concentrations for quantum dot qubits”, *Nat. Commun.* **13**, 7777 (2022) DOI: [10.1038/s41467-022-35510-z](https://doi.org/10.1038/s41467-022-35510-z).
- [39] Y. Feng and R. Joynt, “Enhanced valley splitting in Si layers with oscillatory Ge concentration”, *Phys. Rev. B* **106**, 085304 (2022) DOI: [10.1103/PhysRevB.106.085304](https://doi.org/10.1103/PhysRevB.106.085304).
- [40] M. P. Losert, M. A. Eriksson, R. Joynt, R. Rahman, G. Scappucci, S. N. Coppersmith, and M. Friesen, “Practical strategies for enhancing the valley splitting in Si/SiGe quantum wells”, *Phys. Rev. B* **108**, 125405 (2023) DOI: [10.1103/PhysRevB.108.125405](https://doi.org/10.1103/PhysRevB.108.125405).
- [41] K.-P. Gradwohl, L. Cvitkovich, C.-H. Lu, S. Koelling, M. Oezkent, Y. Liu, D. Waldhör, T. Grasser, Y.-M. Niquet, M. Albrecht, C. Richter, O. Moutanabbir, and J. Martin, “Enhanced nanoscale Ge concentration oscillations in Si/SiGe quantum well through controlled segregation”, *Nano Lett.* **25**, 4204–4210 (2025) DOI: [10.1021/acs.nanolett.4c05326](https://doi.org/10.1021/acs.nanolett.4c05326).
- [42] L. Cvitkovich, T. Salamone, C. Wilhelmer, B. Martinez, T. Grasser, and Y.-M. Niquet, “Valley splittings in Si/SiGe heterostructures from first principles”, (2025) DOI: [10.48550/arXiv.2512.04879](https://doi.org/10.48550/arXiv.2512.04879).
- [43] B. D. Woods, H. Soomro, E. S. Joseph, C. C. D. Frink, R. Joynt, M. A. Eriksson, and M. Friesen, “Coupling conduction-band valleys in modulated SiGe heterostructures via shear strain”, *npj Quantum Inf.* **10**, 54 (2024) DOI: [10.1038/s41534-024-00853-6](https://doi.org/10.1038/s41534-024-00853-6).
- [44] A. Thayil, L. Ermoneit, and M. Kantner, “Theory of valley splitting in Si/SiGe spin-qubits: interplay of strain, resonances and random alloy disorder”, *Phys. Rev. B* **112**, 115303 (2025) DOI: [10.1103/4sdz-f9cr](https://doi.org/10.1103/4sdz-f9cr).
- [45] L. Marcogliese, O. Sabapathy, R. Richter, J.-S. Tu, D. Bougeard, and L. R. Schreiber, “Fabrication, characterization and mechanical loading of si/sige membranes for spin qubit devices”, *arXiv* (2025) DOI: [10.48550/arXiv.2508.14589](https://doi.org/10.48550/arXiv.2508.14589).
- [46] S. F. Neyens, R. H. Foote, B. Thorgrimsson, T. J. Knapp, T. McJunkin, L. M. K. Vandersypen, P. Amin, N. K. Thomas, J. S. Clarke, D. E. Savage, M. G. Lagally, M. Friesen, S. N. Coppersmith, and M. A. Eriksson, “The critical role of substrate disorder in valley splitting in Si quantum wells”, *Appl. Phys. Lett.* **112**, 243107 (2018) DOI: [10.1063/1.5033447](https://doi.org/10.1063/1.5033447).
- [47] A. Hosseinkhani and G. Burkard, “Electromagnetic control of valley splitting in ideal and disordered Si quantum dots”, *Phys. Rev. Research* **2**, 043180 (2020) DOI: [10.1103/PhysRevResearch.2.043180](https://doi.org/10.1103/PhysRevResearch.2.043180).
- [48] L. F. Peña, J. C. Koepke, J. H. Dycus, A. Mounce, A. D. Baczewski, N. T. Jacobson, and E. Bussmann, “Modeling Si/SiGe quantum dot variability induced by interface disorder reconstructed from multiperspective microscopy”, *npj Quantum Inf.* **10**, 33 (2024) DOI: [10.1038/s41534-024-00827-8](https://doi.org/10.1038/s41534-024-00827-8).
- [49] C. H. Yang, A. Rossi, R. Ruskov, N. S. Lai, F. A. Mohiyaddin, S. Lee, C. Tahan, G. Klimeck, A. Morello, and A. S. Dzurak, “Spin-valley lifetimes in a silicon quantum dot with tunable valley splitting”, *Nat. Commun.* **4**, 2069 (2013) DOI: [10.1038/ncomms3069](https://doi.org/10.1038/ncomms3069).
- [50] P. Huang and X. Hu, “Spin relaxation in a Si quantum dot due to spin-valley mixing”, *Phys. Rev. B* **90**, 235315 (2014) DOI: [10.1103/PhysRevB.90.235315](https://doi.org/10.1103/PhysRevB.90.235315).
- [51] A. Hollmann, T. Struck, V. Langrock, A. Schmidbauer, F. Schauer, T. Leonhardt, K. Sawano, H. Riemann, N. V. Abrosimov, D. Bougeard, and L. R. Schreiber, “Large, tunable valley splitting and single-spin relaxation mechanisms in a  $\text{Si/Si}_x\text{Ge}_{1-x}$  quantum dot”, *Phys. Rev. Applied* **13**, 034068 (2020) DOI: [10.1103/PhysRevApplied.13.034068](https://doi.org/10.1103/PhysRevApplied.13.034068).
- [52] M. P. Losert, M. Oberländer, J. D. Teske, M. Volmer, L. R. Schreiber, H. Bluhm, S. Coppersmith, and M. Friesen, “Strategies for enhancing spin-shuttling fidelities in Si/SiGe quantum wells with random-alloy disorder”, *PRX Quantum* **5**, 040322 (2024) DOI: [10.1103/PRXQuantum.5.040322](https://doi.org/10.1103/PRXQuantum.5.040322).
- [53] M. Volmer, T. Struck, A. Sala, B. Chen, M. Oberländer, T. Offermann, R. Xue, L. Visser, J.-S. Tu, S. Trellenkamp, L. Cywiński, H. Bluhm, and L. R. Schreiber, “Mapping of valley splitting by conveyor-mode spin-coherent electron shuttling”, *npj Quantum Inf.* **10**, 61 (2024) DOI: [10.1038/s41534-024-00852-7](https://doi.org/10.1038/s41534-024-00852-7).

- [54] Y. Oda, M. P. Losert, and J. P. Kestner, “Suppressing Si valley excitation and valley-induced spin dephasing for long-distance shuttling”, (2024) DOI: [10.48550/arXiv.2411.11695](https://doi.org/10.48550/arXiv.2411.11695).
- [55] M. Veldhorst, H. G. J. Eenink, C. H. Yang, and A. S. Dzurak, “Silicon cmos architecture for a spin-based quantum computer”, *Nat. Commun.* **8**, 1766 (2017) DOI: [10.1038/s41467-017-01905-6](https://doi.org/10.1038/s41467-017-01905-6).
- [56] N. S. Lai, W. H. Lim, C. H. Yang, F. A. Zwanenburg, W. A. Coish, F. Gassemi, A. Morello, and A. S. Dzurak, “Pauli spin blockade in a highly tunable silicon double quantum dot”, *Sci. Rep.* **1**, 110 (2011) DOI: [10.1038/srep00110](https://doi.org/10.1038/srep00110).
- [57] C. G. Van de Walle and R. M. Martin, “Theoretical calculations of heterojunction discontinuities in the Si/Ge system”, *Phys. Rev. B* **34**, 5621–5634 (1986) DOI: [10.1103/PhysRevB.34.5621](https://doi.org/10.1103/PhysRevB.34.5621).
- [58] A. L. Saraiva, M. J. Calderón, X. Hu, S. Das Sarma, and B. Koiller, “Physical mechanisms of interface-mediated intervalley coupling in Si”, *Phys. Rev. B* **80**, 081305 (2009) DOI: [10.1103/PhysRevB.80.081305](https://doi.org/10.1103/PhysRevB.80.081305).
- [59] M. Friesen, S. Chutia, C. Tahan, and S. N. Coppersmith, “Valley splitting theory of SiGe/Si/SiGe quantum wells”, *Phys. Rev. B* **75**, 115318 (2007) DOI: [10.1103/PhysRevB.75.115318](https://doi.org/10.1103/PhysRevB.75.115318).
- [60] N. Ciroth, A. Sala, R. Xue, L. Ermoneit, T. Koprucki, M. Kantner, and L. R. Schreiber, “Numerical simulation of coherent spin-shuttling in a QuBus with charged defects”, (2025) DOI: [10.48550/arXiv.2512.03588](https://doi.org/10.48550/arXiv.2512.03588).
- [61] M. M. Rieger and P. Vogl, “Electronic-band parameters in strained  $\text{Si}_{1-x}\text{Ge}_x$  alloys on  $\text{Si}_{1-y}\text{Ge}_y$  substrates”, *Phys. Rev. B* **48**, 14276–14287 (1993) DOI: [10.1103/PhysRevB.48.14276](https://doi.org/10.1103/PhysRevB.48.14276).
- [62] E. Ungersboeck, S. Dhar, G. Karlowatz, V. Sverdlov, H. Kosina, and S. Selberherr, “The effect of general strain on the band structure and electron mobility of silicon”, *IEEE Trans. Electron Devices* **54**, 2183–2190 (2007) DOI: [10.1109/TED.2007.902880](https://doi.org/10.1109/TED.2007.902880).
- [63] M. V. Fischetti and S. E. Laux, “Band structure, deformation potentials, and carrier mobility in strained Si, Ge, and SiGe alloys”, *J. Appl. Phys.* **80**, 2234–2252 (1996) DOI: [10.1063/1.363052](https://doi.org/10.1063/1.363052).
- [64] J. Werschnik and E. K. U. Gross, “Quantum optimal control theory”, *J. Phys. B: At., Mol. Opt. Phys.* **40**, R175–R211 (2007) DOI: [10.1088/0953-4075/40/18/R01](https://doi.org/10.1088/0953-4075/40/18/R01).
- [65] P. Gross, D. Neuhauser, and H. Rabitz, “Optimal control of curve-crossing systems”, *J. Chem. Phys.* **96**, 2834–2845 (1992) DOI: [10.1063/1.461980](https://doi.org/10.1063/1.461980).
- [66] J. Nocedal and S. J. Wright, *Numerical optimization*, 2nd ed., Springer Series in Operations Research and Financial Engineering (Springer, New York, 2006), DOI: [10.1007/978-0-387-40065-5](https://doi.org/10.1007/978-0-387-40065-5).
- [67] B. D. Woods, M. A. Eriksson, R. Joynt, and M. Friesen, “Spin-orbit enhancement in Si/SiGe heterostructures with oscillating Ge concentration”, *Phys. Rev. B* **107**, 035418 (2023) DOI: [10.1103/PhysRevB.107.035418](https://doi.org/10.1103/PhysRevB.107.035418).
- [68] Z. Shi, C. B. Simmons, J. R. Prance, J. K. Gamble, T. S. Koh, Y.-P. Shim, X. Hu, D. E. Savage, M. G. Lagally, M. A. Eriksson, M. Friesen, and S. N. Coppersmith, “Fast hybrid silicon double-quantum-dot qubit”, *Phys. Rev. Lett.* **108**, 140503 (2012) DOI: [10.1103/PhysRevLett.108.140503](https://doi.org/10.1103/PhysRevLett.108.140503).
- [69] D. Kim, D. R. Ward, C. B. Simmons, D. E. Savage, M. G. Lagally, M. Friesen, S. N. Coppersmith, and M. A. Eriksson, “High-fidelity resonant gating of a silicon-based quantum dot hybrid qubit”, *npj Quantum Inf.* **1** (2015) DOI: [10.1038/npjqi.2015.4](https://doi.org/10.1038/npjqi.2015.4).